ADVANCED MATERIALS INTERFACES
Open Access
www.advmatinterfaces.de

Check for updates

Hierarchical Surface Restructuring of Ultra-Thin Electrodes and Microelectrode Arrays for Neural Interfacing with Peripheral and Central Nervous Systems

Alexander Blagojevic, Wesley Seche, Hongbin Choi, Skyler L. Davis, Sahar Elyahoodayan, Gregory A. Caputo, Terry C. Lowe, Pouya Tavousi, Sina Shahbazmohamadi, and Shahram Amini**

Long-term implantable neural interfacing devices are crucial in neurostimulation for treating various neurological disorders. These devices rely heavily on electrodes and microelectrode arrays. As the invasiveness of these electrodes increases—particularly for peripheral and central nervous system applications—both potential benefits and risks of adverse side effects to the patient rise. To mitigate risks and enhance device performance and longevity, electrodes for such invasive applications must be thin, flexible, and have small contacts. However, these features typically reduce the geometric surface area and electrochemical performance of the electrodes, diminishing treatment benefits. This report explores the feasibility and advantages of using femtosecond laser hierarchical surface restructuring (HSR) technology to improve electrochemical performance without compromising the structural integrity of ultra-thin (<25 µm) platinum-iridium alloy (Pt10Ir) electrode contacts. In this report, an HSR process is developed that significantly enhances the electrochemical performance of 20 µm thick Pt10Ir electrodes by controlling the depth of restructuring. A comprehensive characterization is conducted to assess the surface, sub-surface, morphological, microstructural, and electrochemical properties of these restructured electrodes using multiple characterization modalities. This evaluation aimed to assess the electrodes' performance and to identify features that promote efficient electron transfer, high electrochemical surface area, excellent electrochemical performance, and biocompatibility.

1. Introduction

Implantable neural interfacing devices function by inhibition, stimulation, modification, alteration or modulation of living neural tissue through targeted delivery of electrical stimulation to specific neurological sites in the human body. Some examples of these devices include but are not limited to neurostimulation devices[1–12] such as spinal cord stimulators,[13–19] sacral nerve stimulators,[20–25] Vagus nerve stimulators,[26–31] deep brain stimulators[32] responsive neurostimulators[33] as well as cardiac rhythm management devices,[34–39] Cochlear implants[40–43] and retinal and bionic vision prosthesis.[4,41,44–50] The electrodes and microelectrode arrays which interface with and transfer charge to neurons or tissue are fundamental to the functionality of all these devices, and there are several interdependent factors to consider when designing and selecting electrode materials.[51,52]

A. Blagojevic, H. Choi, P. Tavousi, S. Shahbazmohamadi, S. Amini
Biomedical Engineering Department
University of Connecticut
Storrs, CT 06269, USA
E-mail: sina@uconn.edu; samini@pulsetechnologies.com

W. Seche, S. Amini
Pulse Technologies Inc.
Research & Development
Quakertown, PA 18951, USA

S. L. Davis, T. C. Lowe
Department of Metallurgical & Materials Engineering
Colorado School of Mines
Golden, CO 80401, USA

S. Elyahoodayan
Department of Biomedical Engineering
University of Southern California
Los Angeles, CA 90089, USA

G. A. Caputo
Department of Chemistry & Biochemistry
Rowan University
Glassboro, NJ 08028, USA

The ORCID identification number(s) for the author(s) of this article can be found under https://doi.org/10.1002/admi.202400017

© 2024 Pulse Technologies Inc. Advanced Materials Interfaces published by Wiley-VCH GmbH. This is an open access article under the terms of the Creative Commons Attribution License, which permits use, distribution and reproduction in any medium, provided the original work is properly cited.

DOI: 10.1002/admi.202400017

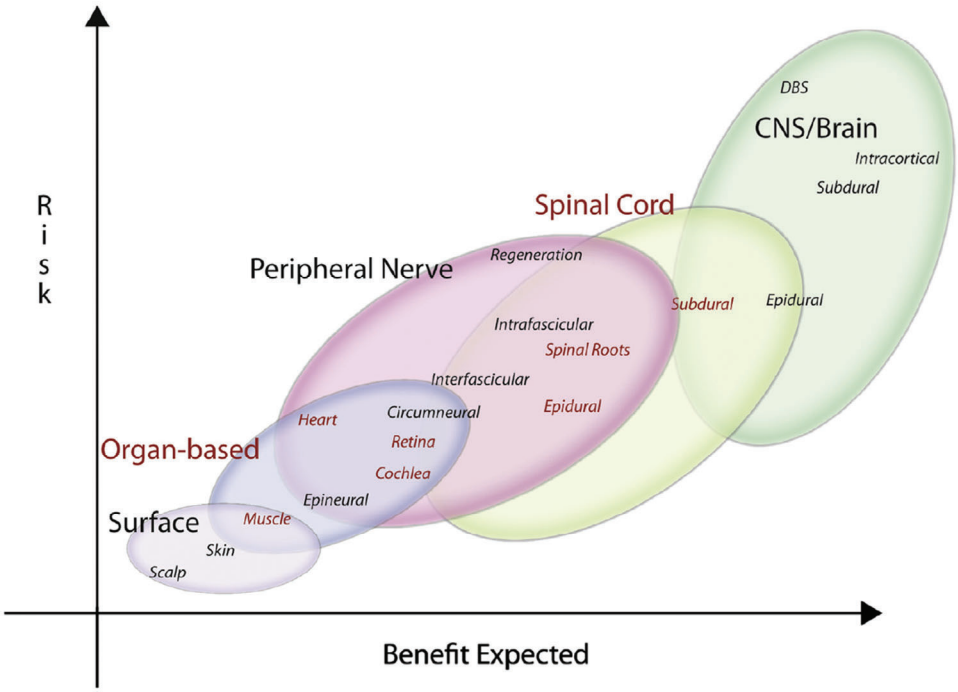

Figure 1. Risk versus potential benefits of neural interfacing electrodes and microelectrode arrays demonstrating that greater invasiveness is often accompanied by greater benefits for the patients; (Photo reproduced with permission from Krames, E.).[51]

These include the target application, stimulation site, electrode size, geometry, material composition, mechanical characteristics, longevity, and density of electrode contacts in an array, as well as their electrochemical properties. There are many examples of electrodes and microelectrode arrays for neural interfacing applications that have been developed since the electrical interface to the nervous system was first described by Italian physician and physicist Luigi Galvani in 1791[51,53,54] who investigated the nature and effects of what he conceived to be electricity in animal tissue.

The design, material, geometry, and overall characteristics of electrodes and microelectrode arrays vary vastly as their degree of invasiveness increases.[9,51,55,56] As the electrodes and microelectrode arrays become more invasive, they pose greater associated risks to patients. However, greater invasiveness correlates with a potentially more intimate interface with the nervous system and, therefore, greater benefit to the patient. This correlation is demonstrated in **Figure 1**[51] which illustrates various locations within the nervous system, each of which require a different type of electrode or microelectrode array.

Surface electrodes,[51,57,58] organ-based electrodes[51] (muscle,[59–61] cochlea,[42,43,62] retina),[45,46,48,50,63] peripheral nervous system (PNS) electrodes,[51,64–66] and central nervous system (CNS) electrodes[51,67] are amongst the most prevalent types of electrodes and microelectrode arrays. This list, though not exhaustive, demonstrates several methods for neural interfacing at different locations within the nervous system. Surface electrodes are relatively simple and pose negligible risks. They are applied to the skin for neurostimulation applications and diagnostic procedures such as electrocardiographic (ECG/EKG) and electroencephalography (EEG),[68,69] transcutaneous electrical nerve stimulation for pain management and physical therapy,[70,71] and electromyography recordings[72] for control of amputee prostheses. Muscle-based electrodes are placed at motor points to activate and stimulate muscles.[59,60,61] Cochlear electrodes stimulate auditory nerves within the cochlea,[40–43,51] and retinal electrodes stimulate the inner retina.[4,41,44–50] PNS electrodes are designed in a number of shapes and geometries (e.g., cuff electrodes[73] or Utah electrode arrays)[74] and are designed for implantation directly interacting with PNS nerves. CNS electrodes, the most invasive types, can be categorized into three groups: 1) Superficial and distal CNS electrodes:[51,75] These include electrodes for stimulating and recording from the brain surface[76] (electrocorticography, a.k.a. ECoG)[77–79] and spinal cord, or for sacral root stimulation to restore bladder and bowel function after spinal cord injury[51,80–82] (**Figure 2**). Over the past two decades, ECoG has become a promising platform for brain-computer interfaces (BCI)[83] requiring electrodes with high spatial resolution, signal fidelity, high signal-to-noise ratio, and durability;[77] 2) Deeper CNS electrodes and microelectrode arrays: These are more complex in their design and manufacturing compared to other CNS and PNS electrodes, as they are intended to be implanted deep within the CNS neural network. These electrodes, such as the ultrafine, hair-like electrodes that have been used in the spinal cord network to interact with individual or very small populations of neurons, are much more invasive.[51,84,85] Cortical electrodes and microelectrode arrays extend ≈5 mm from the surface of the cortex and interact with columnar neuron structures or individual neurons for control of prosthetic limbs and restoring sensation and communication, amongst other functions. They are designed with various geometries and dimensions, generally in the 25–150 µm range

© 2024 Pulse Technologies Inc. Advanced Materials Interfaces published by Wiley-VCH GmbH

21967350, 0, Downloaded from https://onlinelibrary.wiley.com/doi/10.1002/admi.202400017, Wiley Online Library on [19/07/2024]. See the Terms and Conditions (https://onlinelibrary.wiley.com/terms-and-conditions) on Wiley Online Library for rules of use; OA articles are governed by the applicable Creative Commons License

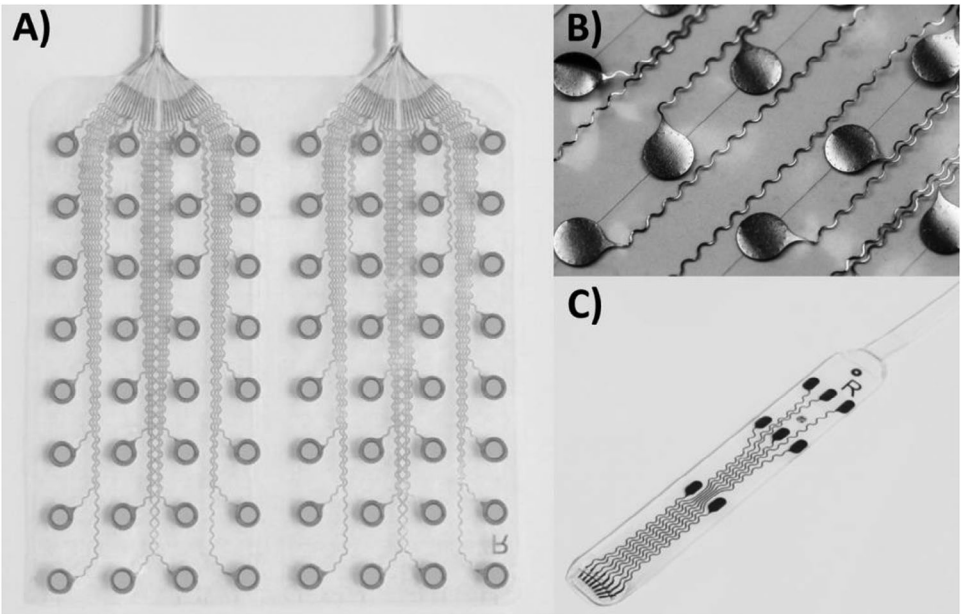

Figure 2. Examples of various geometries and arrangements of commercially available microelectrode arrays with ultra-thin electrode contacts used for recording and stimulation of neural tissue; A & B) CorTec AirRay cortical grid microelectrode array and its Pt10Ir electrode contacts used for ECoG applications; C) CorTec AirRay paddle microelectrode array used for spinal cord stimulation (images used with permission and courtesy of CorTec).

in diameter (e.g., in microwires or needles) or thickness (in thin foils);[86–91] 3) Deep brain stimulation (DBS) electrodes: These are implanted deep into the cortex to modulate the basal ganglia and subthalamic nucleus, treating movement and neurological disorders such as Parkinson's disease, essential tremor, depression, dementia, and epilepsy[32,51,75,92] (Figure S1A,B, Supporting Information).[32,93] DBS electrodes, typically made from cylindrical and shaft-style Pt, Pt10Ir, or Ir, have wall thicknesses and diameters ranging from 25 to 100 µm. Despite DBS's effectiveness, its invasive nature and associated risks have slowed clinical progress. However, recent neural engineering advances, such as current steering or directional stimulation, have led to more targeted modulation of deep brain neural tissues. This is achieved using microelectrode arrays with ultra-thin electrode contacts (<25 µm thick),[94,95] providing smaller geometric surface areas but more electrode contacts[32,51,75,92] for improved stimulation precision, spatial specificity, and accuracy during subthalamic nucleus stimulation[96,97] (Figure S1C, Supporting Information).[32,93]

As outlined earlier, ideal electrode contacts for invasive PNS or CNS applications, such as DBS or BCI, should have very small geometric surface areas, ultra-thin thickness (<25 µm), and mechanical properties congruent with neural tissue. These electrodes must adapt to the spherical shape and irregularities of the brain or subthalamic nucleus, which is best achieved by reducing electrode thickness. This reduction improves patient comfort and device lifespan by increasing conformality and flexibility, reducing friction (against surrounding brain tissue) and trauma, and decreasing the body's immune response.[98–101] Additionally, the electrodes must be biocompatible, reliable over long periods, and have high electrochemical performance. Having said that, increasing the density of electrodes in a target area tends to be accompanied by a reduction in electrode size and geometric surface area. This reduction in surface area reduces the amount of charge that can be delivered per electrode, which adversely decreases the electrochemical performance of electrodes. To overcome this tradeoff, the alternative approach is to enhance the electrochemically active surface area of the electrodes.[9,56,102–107] By maximizing electrochemical surface area, while minimizing geometric surface area, more electrodes can be accommodated in the array thus improving charge storage/injection capabilities, enhancing performance, specificity, selectivity, and signal fidelity. However, a commercially viable technology that achieves these properties has been elusive for decades.[51]

Recent reports demonstrated that femtosecond laser hierarchical surface restructuring (HSR) significantly enhances the electrochemical performance and antibacterial properties of Pt10Ir alloy electrode contacts over 50 µm thick.[56,107] This method yields electrochemical performance superior to most commonly used electrode materials.[9,56,107–112] This enhancement enables further miniaturization of electrodes, allowing higher density of electrodes implanted near target neural tissue for better spatial resolution and specificity.[113,114] This advancement supports the development of minimally invasive electrodes and microelectrode arrays for PNS and CNS interfacing[115] The use of ultra-thin, conformal and flexible electrode contacts also facilitates novel manufacturing techniques, such as fabricating arrays for directional stimulation for use in deep brain stimulation (DBS).[32,116–118]

1.1. Objectives

This work aims to explore the feasibility and advantages of using femtosecond laser HSR technology for hierarchical surface restructuring of ultra-thin (<25 µm) Pt10Ir electrode contacts.

 © 2024 Pulse Technologies Inc. Advanced Materials Interfaces published by Wiley-VCH GmbH

21967350, 0, Downloaded from https://onlinelibrary.wiley.com/doi/10.1002/admi.202400017, Wiley Online Library on [19/07/2024]. See the Terms and Conditions (https://onlinelibrary.wiley.com/terms-and-conditions) on Wiley Online Library for rules of use; OA articles are governed by the applicable Creative Commons License

These electrodes are intended for invasive neural interfacing with the PNS and CNS. Previously, HSR technology has been successfully employed as a robust, cost-effective, and commercially viable surface modification technique on various electrode shapes and geometries for neural interfacing applications.[56,107] These include cylindrical and helical Pt10Ir electrodes for cardiac rhythm management, rivet-style Pt10Ir electrodes for electrophysiology mapping catheters, and cylindrical and paddle Pt10Ir electrodes for spinal cord stimulation arrays. However, the electrodes in these studies had thicknesses in the 100–300 µm range.[56,107,119] Since the HSR technique is a semi-ablative process where the electrode surface undergoes topographical changes driven by both "surface restructuring" and "ablation", it is crucial to fine-tune femtosecond laser HSR parameters to avoid compromising the structural integrity and functionality of ultra-thin (<25 µm) electrodes. In previous works,[56,107] the depth of restructuring was reported to be ≈30–50 µm (Figure S2, Supporting Information), posing no risk to the structural integrity of thicker (100–300 µm) electrodes. For ultra-thin Pt10Ir electrodes, however, the depth of restructuring must be well-controlled and considerably smaller than the electrode thickness.

The thinnest commercially available Pt10Ir foil commonly used in the fabrication of electrodes and microelectrode arrays is 20 µm thick sheets of Pt10Ir manufactured via cold-rolling. Thus, this work reports a methodical approach to regulating the depth of restructuring in a 20 µm thick Pt10Ir electrode by tuning the laser fluence during the HSR process. Laser fluence, which refers to the energy delivered by the laser per unit area, is a crucial parameter that affects how energy is distributed across the surface. We have demonstrated that this controlled and tunable process can enhance the electrochemical performance of ultra-thin 20 µm electrodes by two orders of magnitude while significantly reducing the depth of restructuring relative to the electrode thickness. We studied the surface, sub-surface, morphological, microstructural, and electrochemical properties of these hierarchically restructured ultra-thin Pt10Ir electrodes using multiple modalities of microscopy, spectroscopy, and electrochemical measurement techniques. Additionally, biocompatibility studies (cytotoxicity, irritation, and skin sensitization) were performed to ensure that the restructured electrodes did not elicit any harmful biological reactions.

2. Experimental Section

2.1. Electrode Fabrication via Femtosecond Laser Hierarchical Surface Restructuring (HSR)

The laser source used in these experiments was a Monaco 1035 (Coherent, Santa Clara, CA, USA), that generates 257 fs pulses with a central wavelength of 1035 nm and an initial beam diameter of 2.7 mm. A telecentric, f-theta lens (Wavelength, Singapore) with a focal length of 70 mm focuses the beam down to an ≈8 µm spot size at the focal point. The beam was deflected and targeted via an IntelliSCAN galvo scan head (SCANLAB, Pucheim, Germany). The experiments were performed in an ambient air environment. Electrodes were mounted on a porous, ceramic vacuum chuck with 3D stage controls (Zaber, Vancouver, BC, Canada), and were leveled with the focal plane of the scan-head using a Keyence Confocal Displacement Sensor (Keyence, Osaka, Japan). Targeting and alignment of the pattern to the electrodes was done via a digital microscope (Dino-Lite, Torrance, CA, USA).

Different applications of electrode and microelectrode arrays require different standards and requirements for electrochemical performance. As reported previously[56] the performance of HSR treated electrodes can be tuned by adjusting various laser parameters, offering a degree of flexibility useful to researchers and device manufacturers. Although this performance was a function of many interdependent variables, this work would primarily focus on effective laser fluence, as it had utility in most commercially available lasers. Effective fluence refers to the energy delivered by the laser per unit area and the spatial distribution of that energy across a surface, as defined in Equation 1. In general, it was found that reducing the laser energy by using an average power lower than what was utilized in previous work[56] tended to result in a shallower depth of restructuring. However, solely decreasing average power would dramatically decrease the fluence, which corresponds with poor electrochemical performance.[56] To compensate for this reduced performance, the laser pulse overlap was simultaneously increased to keep the average power low with a higher effective fluence, reducing the performance drop. Pulse overlap (**Figure 3**) refers to the degree to which consecutive laser pulses irradiate the same region and is a function of spatial and temporal laser parameters, including spot size, pulsing frequency, and scan speed. In this research, three HSR electrodes were fabricated at eight effective laser fluences of 0.56, 0.65, 0.80, 1.04, 1.53, 1.89, 2.49, and 3.70 kJ cm^{-2}. Electrodes were fabricated using 20 µm thick Pt10Ir foils (Johnson Matthey Inc., USA) and cut into 5 mm diameter disc-shaped electrodes, with the full surface area of one face of the electrode being completely restructured.

$$\textit{Effective Fluence}\left(\frac{J}{cm^2}\right) = \frac{\textit{Average Power of Laser}\ (W)}{\textit{Laser Spot Size}\ (cm^2)} * \textit{Processing Time}\ (s) \quad (1)$$

Additionally, as a case study meant to explore the feasibility of the HSR technique on a commercially available microelectrode array with ultra-thin electrode contacts, the technique was applied to a cortical grid electrode. The electrode array was mounted onto the vacuum chuck and processed in a similar way as the electrodes restructured in this work. The electrode contacts were ultra-thin (20 µm thick) Pt10Ir alloy. The focal point of the laser was tuned to the center of the circular electrode contact, and the microscope was used to align the HSR pattern to the shape of the electrode contact. The goal of this case study was to maximize the area utilized for HSR, while avoiding laser-induced damage to the surrounding polymer insulation. For this reason, the diameter of the restructured area was reduced by ≈100 µm from the full diameter of the electrode contact to provide a margin for error. Restructuring was done at 0.65 kJ cm^{-2}.

2.2. Scanning Electron Microscopy and Focused Ion Beam Cross Sectioning

Restructured electrodes were imaged using a scanning electron microscope (SEM), assisted by a gallium focused ion beam (FIB) to produce vertical cross sections of the electrodes. SEM and FIB imaging were done using a ZEISS Crossbeam 340 (ZEISS, Oberkochen, Germany) instrument. In previous work, an

© 2024 Pulse Technologies Inc. Advanced Materials Interfaces published by Wiley-VCH GmbH

21967350, 0, Downloaded from https://onlinelibrary.wiley.com/doi/10.1002/admi.202400017, Wiley Online Library on [19/07/2024]. See the Terms and Conditions (https://onlinelibrary.wiley.com/terms-and-conditions) on Wiley Online Library for rules of use; OA articles are governed by the applicable Creative Commons License

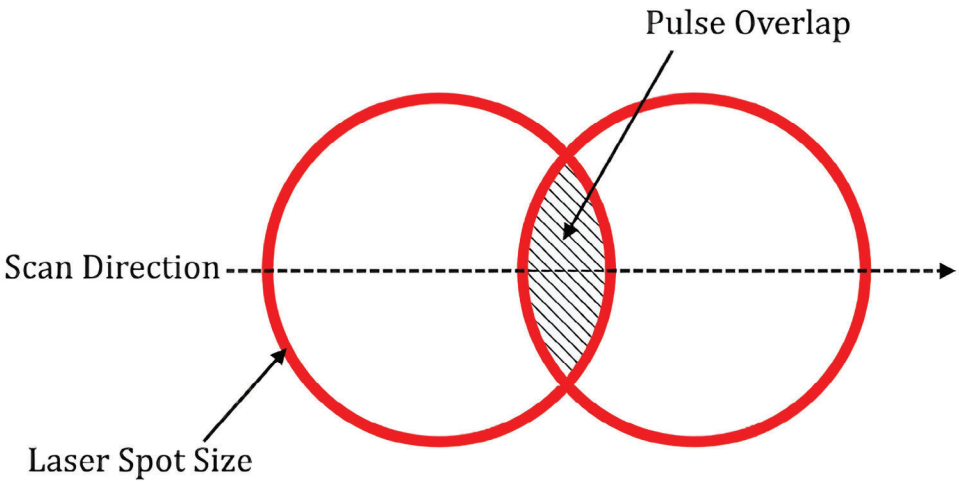

Figure 3. An illustration of successive laser pulses and their overlapping region.

optical surface profiler was used to quantify height information from the surfaces of the hierarchically restructured electrodes, but this profiler was unable to capture the depth of restructuring or subsurface features.[56] For this reason, FIB cross sections were used to accurately characterize the depth of restructuring, including subsurface features. Images were taken with an in-column secondary electron detector at an accelerating voltage of 5 kV. Images were taken at various magnifications and at 0° and 52° tilt to visualize the hierarchical structures at various length scales and in three-dimensions. FIB cross sectioning was performed at 300 pA and an accelerating voltage of 30 kV to create a trench, which revealed subsurface features induced by restructuring. Cross sections were polished with a second pass at 50 pA to ensure clarity of subsurface features. The depth of restructuring was quantified by measuring the distance from the bottom of the electrode to the deepest, restructuring-induced subsurface feature visible in the cross section, and subtracting from the thickness of the unaltered electrode. Cross sections were taken at a slight 15° angle relative to the level of the restructuring pattern to observe subsurface features at different locations in the periodic structure. Due to the significant time required to produce high quality cross sections on a Ga-FIB, only electrodes produced at select fluences were chosen for cross sectioning and subsequent SEM imaging and depth measurements, and only half of each cross section was polished. SEM images of the cross sections were taken at a 54° tilt angle. This approach saved time and resources, while still being able to identify a correlation between depth of restructuring and laser fluence.

2.3. Ion Milling and Electron Backscatter Diffraction (EBSD) Analysis

To prepare the electrodes for Electron Backscatter Diffraction (EBSD) analysis, ion milling was performed using a JEOL IB-09010CP Cross Section Polisher (Tokyo, Japan) for a duration of 5 h with a 5.0 kV accelerating voltage and a 4.5 Argon gas flow resulting in ≈120 µA of current. EBSD of polished cross-sections of three electrodes (i.e., an unrestructured electrode, and electrodes restructured at 0.56 and 2.49 kJ cm^{-2}) was conducted using a JEOL JSM-7000F Field Emission Scanning Electron Microscope (Tokyo, Japan) equipped with an EDAX Hikari Pro 600pps Detector (Mahwah, NJ) to analyze the microstructure, grain size, grain orientation and texture of the electrodes before and after restructuring. Ametek Inc.'s OIM Analysis software (Version 8) was used for EBSD post-processing analysis and image refinement with neighbor pattern average re-indexing, grain dilation, and neighbor confidence index correlation.

2.4. Electrochemical Measurements

Electrochemical performance of the electrodes was assessed via cyclic voltammetry (CV) and electrochemical impedance spectroscopy (EIS) to measure charge storage capacity (CSC), impedance, and specific capacitance (SC).[9,56,104–107] CSC is calculated using the formula described in Equation 2 and SC is calculated by fitting a model of a Randles circuit to EIS data, and normalizing for area. Full CV and EIS experimental details can be found in previous works.[56,107]

$$CSC = \frac{1}{\nu GSA} \int I dt \tag{2}$$

2.5. Biocompatibility Studies

2.5.1. In Vitro Cytotoxicity

Cellular cytotoxicity studies were carried out according to ISO 10993–5:2009E. Briefly, coated electrodes were incubated in complete minimum essential medium (Eagles) with Earle's balanced salts which was supplemented to contain 10% fetal bovine serum at a ratio of 3 cm^2 mL^{-1} of electrode to medium. Pharmacopeia High Density Polyethylene Reference Standard at 3 cm^2 mL^{-1} and latex rubber beads at a ratio of 0.2 cm^2 mL^{-1} were used as negative and positive controls, respectively.[120–123] The extracts were then applied to confluent cell layers of L929 mammalian fibroblasts (*Mus musculus*) at a ratio of 2 mL per 35 mm plate

© 2024 Pulse Technologies Inc. Advanced Materials Interfaces published by Wiley-VCH GmbH

21967350, 0, Downloaded from https://onlinelibrary.wiley.com/doi/10.1002/admi.202400017, Wiley Online Library on [19/07/2024]. See the Terms and Conditions (https://onlinelibrary.wiley.com/terms-and-conditions) on Wiley Online Library for rules of use; OA articles are governed by the applicable Creative Commons License

and allowed to incubate at 37 °C for 48 h. Following incubation, the plates were examined microscopically to determine qualitative morphological reactivity using the scoring system in Table S1 (Supporting Information). Full details on the methodology can be found in the Supporting Information.

2.5.2. In Vivo Reactivity Studies

Intracutaneous (intradermal) reactivity tests were performed based on ISO 10993-10:2010(E). Healthy young adult female albino rabbits from a single strain (New Zealand) weighing not less than 2 kg (Charles River) previously unused for skin irritation studies and whose skin was free from mechanical irritation or trauma were used in this study. Briefly, extracts of the restructured electrodes were prepared in accordance with ISO 10993-12 at a ratio of electrode to extraction medium of 3 cm^2 mL^{-1} for each extraction medium: saline or vegetable oil. Saline and 0.1% sodium dodecyl sulfate in 0.9% sodium chloride were negative and positive controls, respectively. Subjects received 0.2 mL injections intracutaneously at five sites on the left side. Immediate examination and follow-ups at 24 ± 2, 48 ± 2, and 72 ± 2 h post-injection assessed gross evidence of tissue reaction (erythema and edema) scored using the system in Table S2 (Supporting Information). Full details of the methodology can be found in the Supporting Information.

Skin sensitization tests were carried out using the Guinea Pig Maximization Test (GPMT), as defined in ISO 10993-10:2010(E). Healthy, young adult, albino guinea pigs from a single outbred strain (Dunkin Hartley) weighing between 300 and 500 g and previously unused for testing were used. Briefly, extracts were prepared as mentioned above in accordance with ISO 10993-12. Initial injections were done in a single row of three on each side of the midline, within a 4 × 6 cm area. After 1-week, topical inductions were carried out by placing a 2 × 4 cm gel blot paper soaked with the test extract or control over injection sites and then covered with an adhesive bandage. After 15 days, the challenge phase commenced by applying 0.25 mL of extract or controls. Propylene glycol ± 0.1% dinitrochlorobenzene were used as the positive and negative controls. Challenges were applied for 48 h, and assessment of sensitization was carried out using the system in Table S3 (Supporting Information) 48 h after challenge removal. Full details of the methodology can be found in the Supporting Information.

3. Results and Discussion

3.1. Surface and Sub-Surface Characterization

The hierarchical surface restructuring (HSR) technique was successfully employed on the 20 µm thick Pt10Ir electrodes and produced a periodic structure across the surface of the electrodes, as shown in the SEM micrographs of **Figures 4** and **5**. The lower magnification images show coarse-scale pillar structures ≈10–15 µm across, with the spacing between them decreasing from ≈5 µm at 0.56 kJ cm^{-2} to ≈2 µm at 3.70 kJ cm^{-2} fluence. These structures were mostly circular, with a smaller, secondary structure appearing near the top right of each pillar. The higher magnification images show the fine-scale nanostructures on top of the pillars in the range of a few nanometers to a few hundred nanometers.

The depth of restructuring, which is of primary interest, could not be accurately determined from a top-down SEM image alone, due to the poor signal in the valleys between the pillar structures. For this reason, cross sections were made with the Ga-FIB and targeted in the center of the dark valleys, which were assumed to be the deepest part of the valleys. The cross sections (**Figure 6**) provided a detailed view of the structures' cross-sectional peak-valley profile. The depth of restructuring was then characterized as the distance between the deepest part of a valley and the highest point of an adjacent peak, which were found to be approximately level with the unmodified surface surrounding the restructured area of the electrodes. In the low end of the fluence regime, from 0.56 to 0.80 kJ cm^{-2}, much of the valleys between the pillars are clearly visible, as the valleys are relatively shallow. Additionally, in the SEM images of the 0.56 and 0.65 kJ cm^{-2} electrodes as shown in Figure 4, a relatively unrestructured area with a radius of ≈2–2.5 µm was observed in the center of the pillar structures. These areas are relatively unrestructured, likely because they were captured within the relatively low energy beam tail region of the laser spot, which does not have enough energy to significantly alter the surface or ablate material at low fluences. As fluence increased beyond 0.80 kJ cm^{-2}, the frequency of nanoscale structures in these unrestructured regions increased, as well as across the entire surface altogether. Predictably, the depth of restructuring increased as a function of fluence as illustrated in Figure 6, likely attributed to higher fluences increasing the rate of ablation that, in turn, generated deeper valleys between the peaks.

From the FIB cross sections, it was found that the depth of restructuring increased from ≈6.5 µm at 0.56 kJ cm^{-2} fluence to ≈20 µm at 3.70 kJ cm^{-2} fluence. At 3.70 kJ cm^{-2} fluence, the cross section revealed that the laser had fully penetrated the electrodes, with the valleys of the hierarchical structures extending through the full thickness of the electrodes. This electrode would be unviable in a practical application, as it is structurally compromised and too fragile to maintain integrity, and was therefore not studied further in this work. At the second highest fluence tested (2.49 kJ cm^{-2}) the laser did not penetrate the full thickness of the electrodes. It did, however, slightly damage the opposite side of the electrodes by creating distinct, periodic fissures and cracks likely induced by laser-driven shock waves. All other electrodes fabricated with fluences less than 2.49 kJ cm^{-2} showed no signs of warping or damage to the opposite side of the electrodes.

Characterization of the microstructure using EBSD was performed on an unrestructured 20 µm thick Pt10Ir electrode, and two electrodes restructured at 0.56 kJ cm^{-2} fluence and 2.49 kJ cm^{-2} fluence. The inverse pole figure map in **Figure 7a** demonstrates that the unrestructured electrode is comprised of ≈1 µm thick, flat lamellar grain layers approximately parallel to the electrode surface. The grain length in the plain of the electrode exceeds 60 µm. The grains for the restructured electrodes, as observed in Figure 7b,c, are larger in the vertical direction with average measured vertical intercept lengths of 1.63 and 1.08 µm as compared to the average vertical intercept length of 0.91 µm for unrestructured electrodes. The average grain layer thickness increases due to laser restructuring. Horizontal grain boundaries

© 2024 Pulse Technologies Inc. Advanced Materials Interfaces published by Wiley-VCH GmbH

21967350, 0, Downloaded from https://onlinelibrary.wiley.com/doi/10.1002/admi.202400017, Wiley Online Library on [19/07/2024]. See the Terms and Conditions (https://onlinelibrary.wiley.com/terms-and-conditions) on Wiley Online Library for rules of use; OA articles are governed by the applicable Creative Commons License

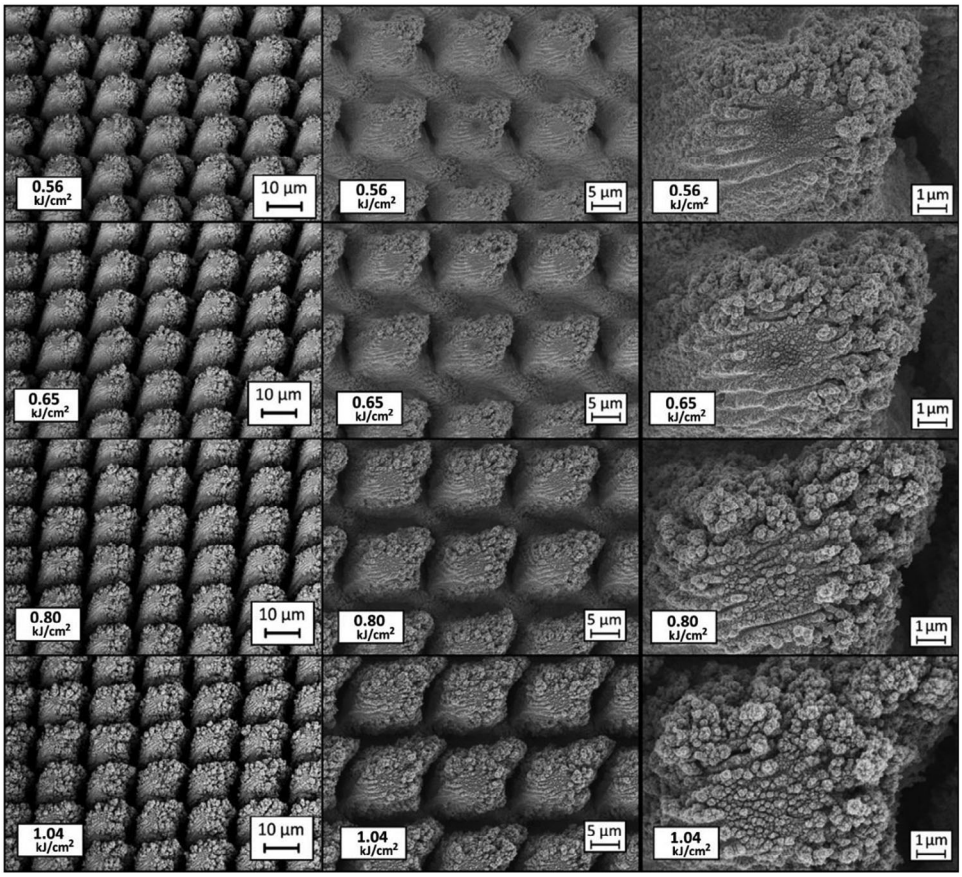

Figure 4. SEM micrographs (taken at 25° tilt angle) of 20 µm thick Pt10Ir electrodes hierarchically restructured with fluences of 0.56, 0.65, 0.80, and 1.04 kJ cm^{-2}.

either migrate or sub-grain boundaries are removed by laser restructuring. The grains appear to continue on either side of the valleys created during laser restructuring. The grains in the restructured electrode at 0.56 kJ cm^{-2} fluence developed curvature near the laser-exposed free surfaces close to the base of the valleys, whereas for the restructured electrode at 2.49 kJ cm^{-2} fluence the grains remain planar and parallel to the electrode surface. There is a high density of low energy boundaries with low misorientation angles (<7.5°) in all electrodes as demonstrated in the grain boundary misorientation maps in **Figure 8**. There is an apparent high density of closely spaced low-angle grain boundaries, as seen by the large number of predominantly horizontal green lines in the unrestructured substrate (Figure 8a) that are retained after restructuring (Figures 8b and 10c). Low-angle grain boundaries, also known as sub-grain boundaries, are defined as boundaries with a misorientation angle <15°. Low-angle grain boundaries are typically composed of ordered dislocation arrays. The inverse pole figures for all three electrodes appear in **Figure 9**. All of the inverse pole figure maps show crystallographic layers, but with no strong relationship of the crystal orientations before and after laser restructuring. There is a tendency for the FCC cubic directions to lie in the plane parallel to the original surface in the unrestructured 20 µm thick Pt10Ir electrode. This [001] texture remains in the electrodes restructured with 0.56 and 2.49 kJ cm^{-2} fluences. However, grains which had[101] orientations in the unrestructured 20 µm thick Pt10Ir electrode are replaced by grains with a moderate tendency to have either their[111] or[112] directions lie in the plane parallel to the electrode surface for the electrodes restructured with fluences of 0.56 and 2.49 kJ cm^{-2}, respectively.

3.2. Electrochemical Performance Measurements

To quantify the performance of the hierarchically restructured ultra-thin electrodes, cyclic voltammograms of the electrodes (**Figure 10A**) were plotted and compared to an unrestructured ultra-thin Pt10Ir electrode of the same thickness (20 µm) (inset of Figure 10A). Total charge storage capacity (CSC_t) was calculated and normalized by integrating the area within the cyclic voltammograms and dividing by the exposed geometric surface area of the electrodes in the electrochemical test cell. It is evident from Figure 10A,b that CSC_t can be tuned by adjusting fluence, with higher fluences corresponding to a greater depth of restructuring and, consequently, higher electrochemical performance. The increased depth of restructuring contributes to higher performance by producing a greater electrochemical surface area utilized for electrochemical reactions and increased density of restructured surfaces. It follows that maximum performance is constrained by the thickness of the electrodes. Regardless, at the low end

 © 2024 Pulse Technologies Inc. Advanced Materials Interfaces published by Wiley-VCH GmbH

21967350, 0, Downloaded from https://onlinelibrary.wiley.com/doi/10.1002/admi.202400017, Wiley Online Library on [19/07/2024]. See the Terms and Conditions (https://onlinelibrary.wiley.com/terms-and-conditions) on Wiley Online Library for rules of use; OA articles are governed by the applicable Creative Commons License

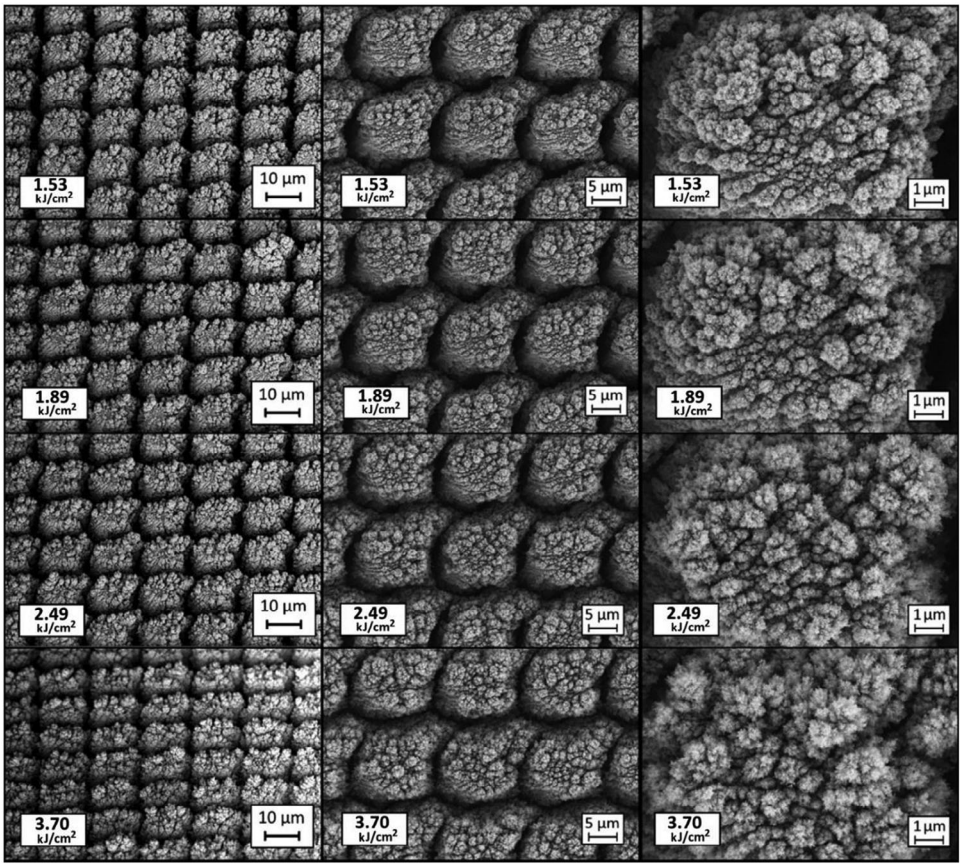

Figure 5. SEM micrographs (taken at 25° tilt angle) of 20 µm thick Pt10Ir electrodes hierarchically restructured with fluences of 1.53, 1.89, 2.49, and 3.70 kJ cm^{-2}.

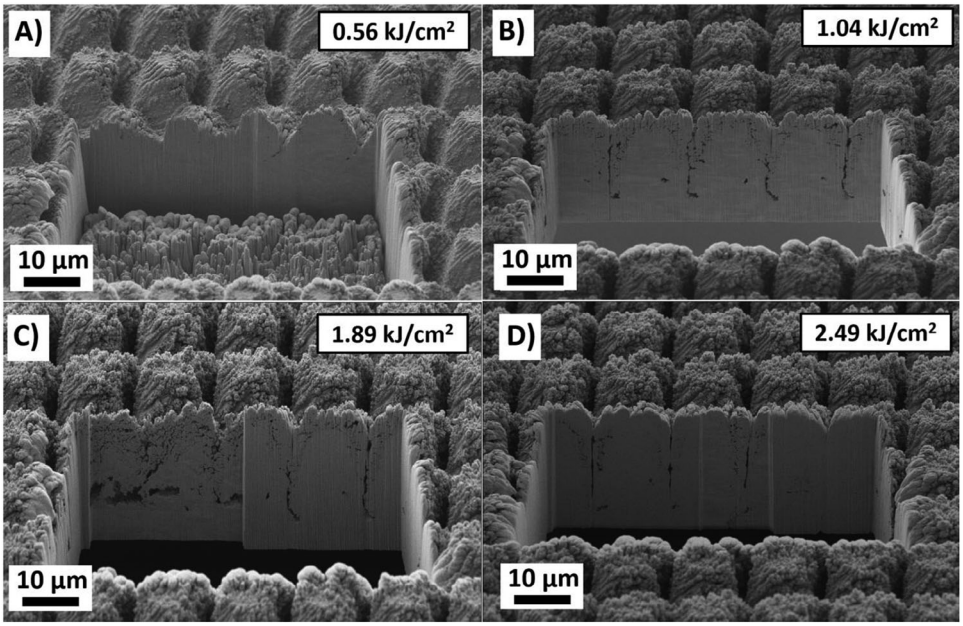

Figure 6. SEM images of FIB cross sections of electrodes fabricated at fluences of, A) 0.56 kJ cm^{-2}, B) 1.04 kJ cm^{-2}, C) 1.89 kJ cm^{-2}, and D) 2.49 kJ cm^{-2} produced with Ga-FIB.

© 2024 Pulse Technologies Inc. Advanced Materials Interfaces published by Wiley-VCH GmbH

21967350, 0, Downloaded from https://onlinelibrary.wiley.com/doi/10.1002/admi.202400017, Wiley Online Library on [19/07/2024]. See the Terms and Conditions (https://onlinelibrary.wiley.com/terms-and-conditions) on Wiley Online Library for rules of use; OA articles are governed by the applicable Creative Commons License

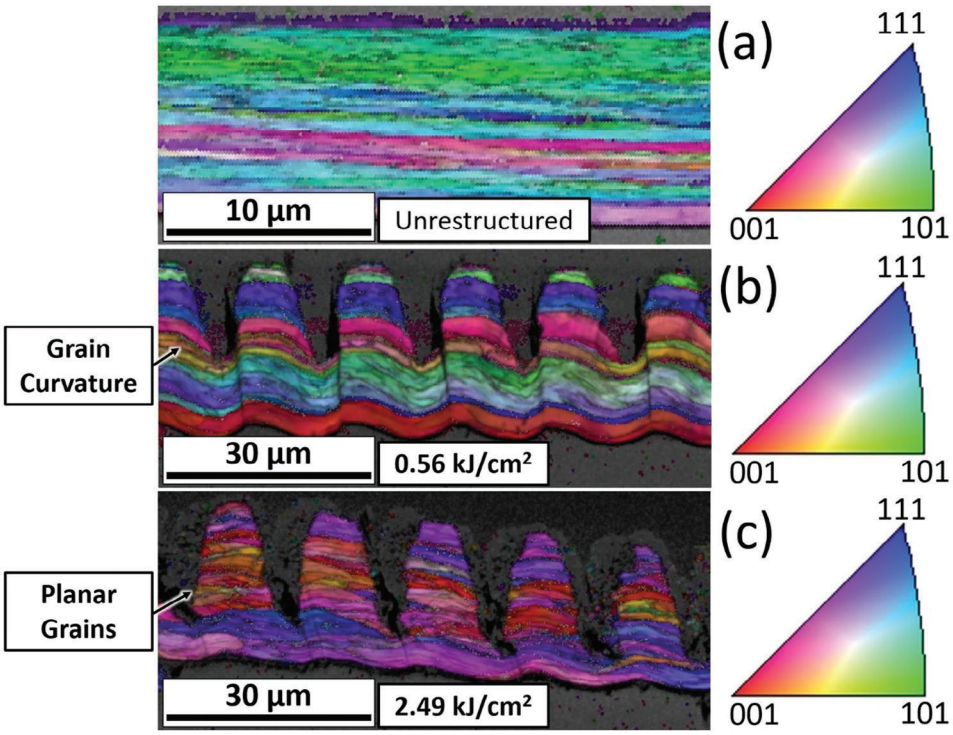

Figure 7. Inverse pole figure maps of, a) unrestructured 20 µm thick Pt10Ir electrode, b) 20 µm thick Pt10Ir electrode restructured with 0.56 kJ cm^{-2} fluence, and, c) 20 µm thick Pt10Ir electrode restructured with 2.49 kJ cm^{-2} fluence.

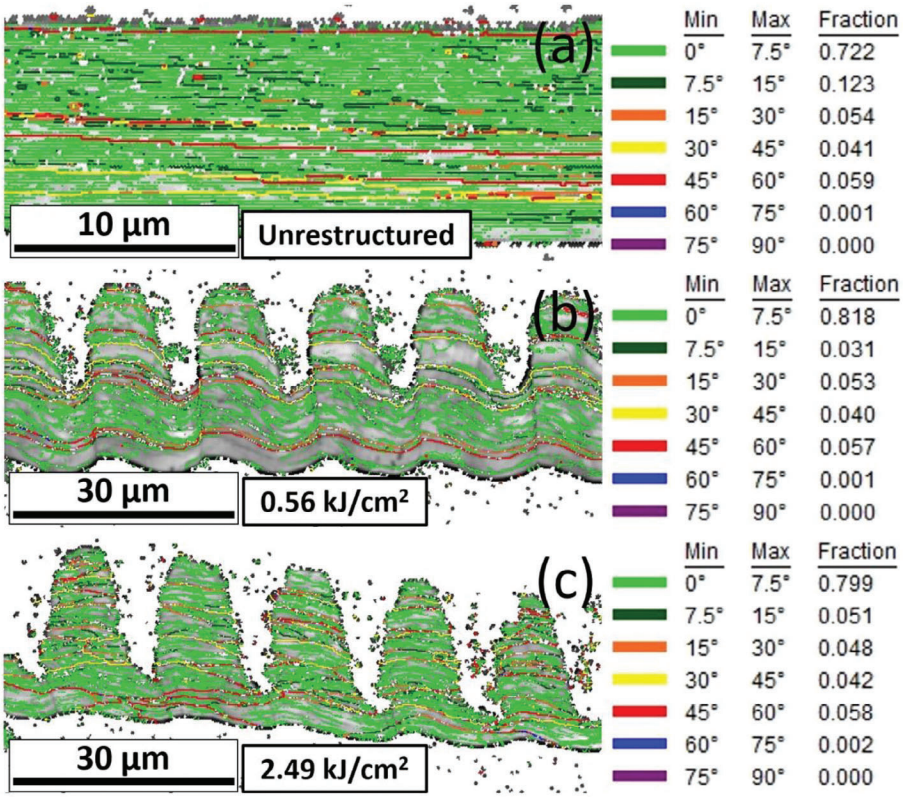

Figure 8. Grain boundary misorientation maps of, a) unrestructured 20 µm thick Pt10Ir electrode, b) 20 µm thick Pt10Ir electrode restructured with 0.56 kJ cm^{-2} fluence, and c) 20 µm thick Pt10Ir electrode restructured with 2.49 kJ cm^{-2} fluence.

 © 2024 Pulse Technologies Inc. Advanced Materials Interfaces published by Wiley-VCH GmbH

21967350, 0, Downloaded from https://onlinelibrary.wiley.com/doi/10.1002/admi.202400017, Wiley Online Library on [19/07/2024]. See the Terms and Conditions (https://onlinelibrary.wiley.com/terms-and-conditions) on Wiley Online Library for rules of use; OA articles are governed by the applicable Creative Commons License

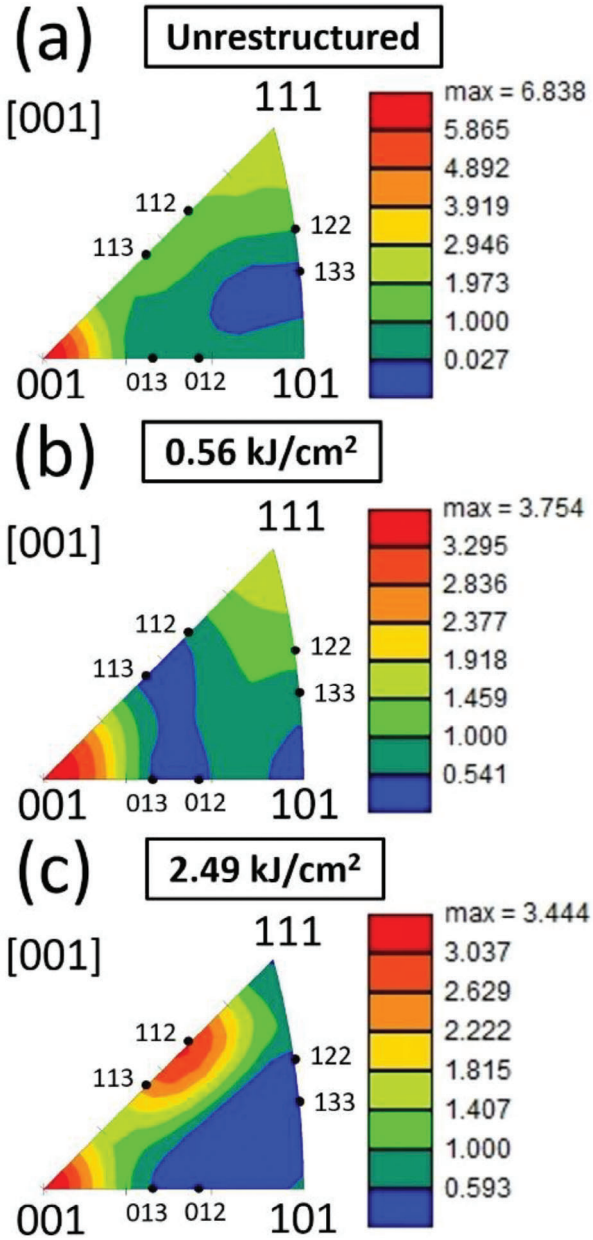

Figure 9. Inverse pole figures of, a) unrestructured 20 µm thick Pt10Ir electrode, b) 20 µm thick Pt10Ir electrode restructured with 0.56 kJ cm^{-2} fluence, and c) 20 µm thick Pt10Ir electrode restructured with 2.49 kJ cm^{-2} fluence.

of the restructuring spectrum, that is, at an applied fluence of 0.56 kJ cm^{-2} with a restructuring depth of ≈6.5 µm, an average CSC$_t$ of 36 mC cm^{-2} was achieved. This represents nearly an 18-fold increase in electrochemical performance compared to an unrestructured ultra-thin Pt10Ir electrode that exhibited an average CSC$_t$ of 2 mC cm^{-2}. The depth of restructuring suggests that even electrodes with thicknesses below 20 µm can be restructured. The highest CSC$_t$ measured was an average of 231 mC cm^{-2} obtained for electrodes restructured at 3.70 kJ cm^{-2} fluence. Although this performance was unprecedented for ultra-thin Pt10Ir electrodes, those electrodes restructured at 3.70 kJ cm^{-2} fluence were structurally unstable due to the laser having penetrated the full thickness of the electrodes rendering them unsuitable for use in practical applications. The next highest performing electrodes that maintained structural integrity were restructured at 2.49 kJ cm^{-2} fluence and exhibited an average CSC$_t$ of 184 mC cm^{-2}, a ≈85-fold increase in performance over an unrestructured electrode.

Electrochemical impedance spectroscopy (EIS) data obtained for unrestructured and restructured ultra-thin Pt10Ir electrodes in room temperature PBS are shown in **Figure 11A** (plotted in the 0.1–10^4 Hz frequency range for select electrodes). The data is presented in bode-plot format with the logarithm of impedance plotted as a function of the logarithm of frequency. The EIS data clearly demonstrates a substantial decrease in impedance in a wide frequency range (0.1–10^3 Hz) for electrodes restructured at various levels of laser fluence compared to the unrestructured Pt10Ir electrode. At the lowest fluence of 0.56 kJ cm^{-2}, there is an approximately one order-of-magnitude reduction in impedance from 0.1–100 Hz compared to the unrestructured electrode. As the laser fluence increases, the decrease in impedance becomes even more pronounced, dropping by two-orders-of-magnitude at fluences greater than 0.65 kJ cm^{-2} in the 0.1–10 Hz range, and then one order-of-magnitude up to 100 Hz. All restructured electrodes still show a significant drop in impedance, up to 1000 Hz. At high frequencies greater than 1000 Hz, electrochemical behavior is mostly governed by electrolyte conductivity, where impedance magnitudes showed solution resistance to be ≈15 Ω.

Additionally, specific capacitance (Figure 11B) was improved in a range from an 80-fold increase at 0.56 kJ cm^{-2} to nearly a 1400-fold increase at 3.70 kJ cm^{-2}, compared to the 0.41 µF mm^{-2} specific capacitance of the unrestructured electrodes. The highest performing and structurally stable electrode (restructured at 2.49 kJ cm^{-2}) exhibited an average specific capacitance of 404 µF mm^{-2}, that is, over three orders-of-magnitude improvement from unrestructured electrodes. Like charge storage capacity, specific capacitance can also be tuned by modifying the laser fluence. As is the case with CSC$_t$, it is imperative to note that the maximum achievable electrochemical performance is constrained by the electrodes' thickness, since charge storage capacity and specific capacitance both correlate with depth of restructuring of the electrodes.

3.3. Case Study: Hierarchical Surface Restructuring of Ultra-Thin Pt10Ir Electrodes in a Cortical Microelectrode Array for Treatment of Epilepsy

Figure 12A shows an ultra-thin (20 µm thick) Pt10Ir electrode contact, which is part of a commercially available cortical grid microelectrode array. This device was used as a case study, to demonstrate the practicality of the HSR technique on an existing prefabricated microelectrode array. The array contained several Pt10Ir electrode interfaces each with a surface area of ≈7mm^2 surrounded by silicone insulation molding. As described in the methodology section of this report, the HSR technique was successfully deployed, restructuring most of the

© 2024 Pulse Technologies Inc. Advanced Materials Interfaces published by Wiley-VCH GmbH

21967350, 0, Downloaded from https://onlinelibrary.wiley.com/doi/10.1002/admi.202400017, Wiley Online Library on [19/07/2024]. See the Terms and Conditions (https://onlinelibrary.wiley.com/terms-and-conditions) on Wiley Online Library for rules of use; OA articles are governed by the applicable Creative Commons License

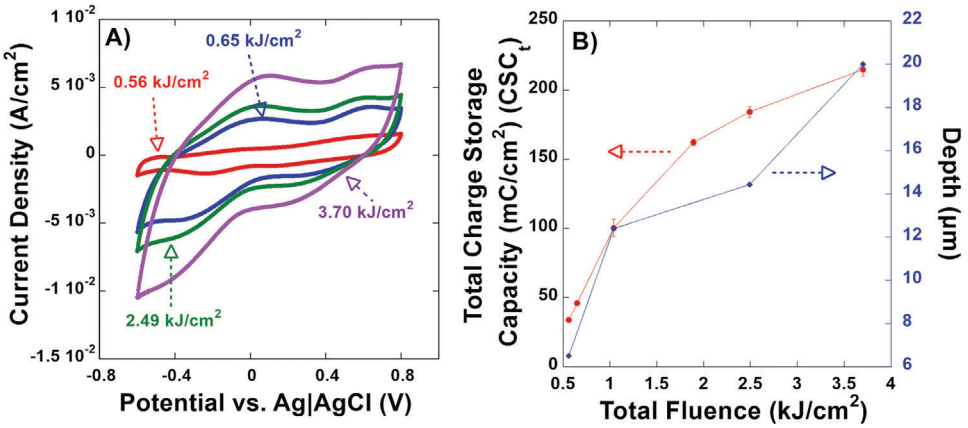

Figure 10. A) Cyclic voltammogram of various restructured electrodes and an unrestructured Pt10Ir electrode (inset) taken from −0.6 to 0.8 V, against an Ag/AgCl reference electrode; B) Total charge storage capacity of electrodes restructured at various fluences plotted against the depth of restructuring of electrodes restructured at 0.56, 1.04, 1.89, and 2.49 kJ cm^{-2}, as measured from FIB cross sections of the electrodes.

electrode contact's area, with no damage to the silicone molding. Inspection of the opposite side of the electrode via light microscope showed no damage as a result of the restructuring process, indicating that the structural stability of the electrode had not been compromised. This electrode contact was restructured using 0.65 kJ cm^{-2} fluence. As it was demonstrated in Figures 10b and 11b, the restructured electrode exhibited a CSC_t of ≈46 mC cm^{-2} and specific capacitance of ≈35 µF mm^{-2}, while maintaining a depth of restructuring under 10 µm. This case study demonstrates that the HSR technique can be adapted to the unique geometric and material constraints of existing commercial microelectrode arrays. Furthermore, it shows that HSR can be integrated as an in-line surface treatment in the electrode manufacturing process. This allows device manufacturers to enhance the electrochemical performance of their devices without significantly altering existing manufacturing infrastructure.

As a final point, for benchmarking the electrochemical performance of ultra-thin HSR Pt10Ir electrodes, we compare them to other high-performing, state-of-the-art electrode coating materials. Due to the variable nature of electrochemical test setups and experimental conditions, quantitative comparisons should be approached with caution since small changes in test parameters can lead to significantly different measurements, even with area normalization. To ensure relevant comparisons, we reference studies using electrochemical measurement parameters (e.g., voltage range, sweep rate, electrolyte) similar to those in this work, to the extent reported in the literature. We have compared materials based on charge storage capacity (CSC), as other metrics like impedance are more challenging to reliably normalize. Several studies were reviewed for each material, but for conciseness, we discuss only the study reporting the highest CSC.

The highest CSC of an HSR electrode reported in this work was 184 mC cm^{-2} (204 mC cm^{-2} if assuming greater risk to structural integrity). In comparison, the best-performing materials in literature were 173 mC cm^{-2} for titanium nitride (TiN) electrodes,[9,56,108,109,111,119,124] 151.2 mC cm^{-2} for PEDOT electrodes,[99,110,125,126] and 388 mC cm^{-2} for iridium oxide (IrO_2) electrodes.[124,127–130] Amongst these, certain IrO_2 films (SIROF,

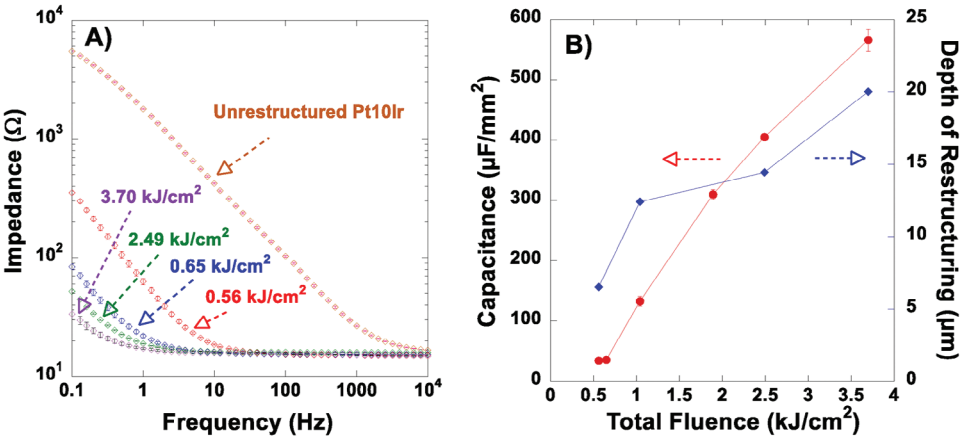

Figure 11. A) Bode plots of impedance magnitude as a function of frequency (plotted in the 0.1–10^4 Hz frequency range) for various restructured electrodes and an unrestructured Pt10Ir electrode; B) Specific capacitance of electrodes restructured at various fluences plotted against the depth of restructuring, as measured from cross sections of the electrodes.

© 2024 Pulse Technologies Inc. Advanced Materials Interfaces published by Wiley-VCH GmbH

21967350, 0, Downloaded from https://onlinelibrary.wiley.com/doi/10.1002/admi.202400017, Wiley Online Library on [19/07/2024]. See the Terms and Conditions (https://onlinelibrary.wiley.com/terms-and-conditions) on Wiley Online Library for rules of use; OA articles are governed by the applicable Creative Commons License

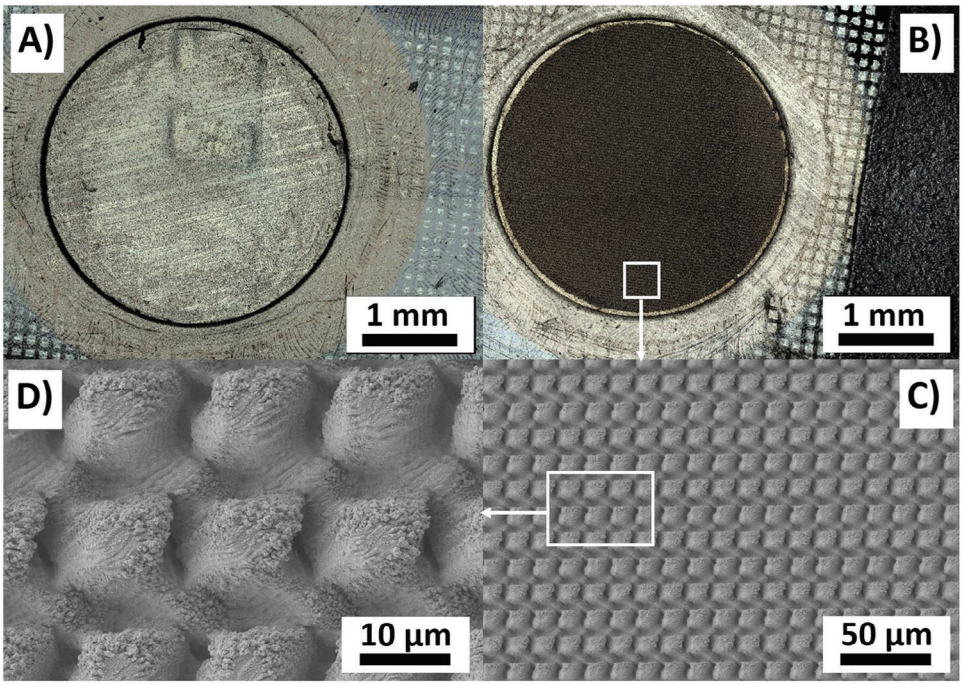

Figure 12. Optical micrograph of an ultra-thin (20 µm) Pt10Ir electrode contact interface of a cortical grid microelectrode array for treatment of epilepsy before A) and after B) hierarchical surface restructuring with 0.65 kJ cm^{-2} fluence; The Pt10Ir electrode contact is surrounded by an insulating silicone molding that is used in the fabrication of the microelectrode array; C,D) SEM micrographs of the surface of the hierarchically restructured ultra-thin (20 µm) Pt10Ir electrode contact at various magnifications clearly demonstrating the hierarchical surface structure induced on the surface of the electrode.

AIROF, etc.) were shown to have outperformed HSR electrodes. While IrO_2 is an excellent conductor with high electrochemical performance, its high cost and the challenges associated with manufacturing iridium targets (due to the brittleness of pure iridium) make it prohibitively expensive.[131] Additionally, the brittle nature of IrO_2 films makes them unsuitable for applications requiring flexible electrodes.[99] In contrast, using HSR on Pt10Ir electrodes is more cost-effective and significantly faster to fabricate compared to the coating processes used for IrO_2 thin films that could potentially take in the upward of several hours. HSR parameters discussed in this study, however, allowed fabrication times in the order of several minutes.

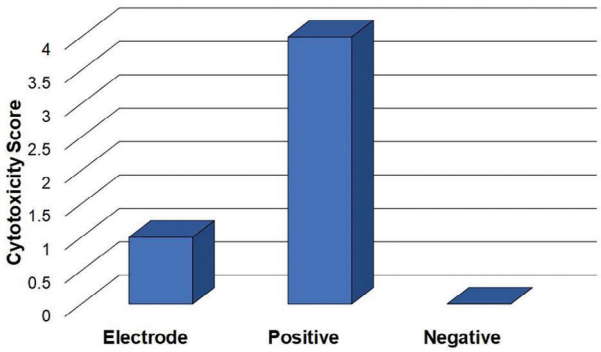

Figure 13. In vitro cytotoxicity assay; Cultures of L929 murine fibroblast cells were exposed to aqueous extracts from restructured Pt10Ir electrodes. Latex microspheres were used as the positive control and the negative control was a similar extract using a USP high-density polyethylene reference standard. Scoring was based on microscopic evaluation of cell and cell-layer morphology. Experiments were performed in triplicate.

While materials such as TiN and PEDOT may not offer the same high electrochemical performance as HSR Pt10Ir electrodes, they have other advantages. These materials, including IrO_2, are typically applied as thin-film coatings, enabling electrode geometries thinner than currently possible with HSR. Some electrodes can be less than 1 µm thick,[130] whereas the thinnest HSR electrode demonstrated so far is 20 µm thick. Despite the greater thickness, HSR still provides a competitively low profile compared to other manufacturing techniques. The greatest advantage of HSR is its ability to deliver similar or better performance than most modern, high-performing materials while being more cost-effective in terms of materials, labor, and manufacturing time. As shown in the case study, HSR is particularly attractive to medical device manufacturers already using Pt10Ir electrode contacts, as it can be easily integrated into existing assembly lines, further saving time and money.

3.4. Biocompatibility Studies

Biocompatibility was assessed using three independent assays—a cell culture cytotoxicity assay (ISO 10993–5), an intradermal (intracutaneous) irritation test using a rabbit model system (ISO 10993-10), and a skin sensitization test using a guinea pig model system (ISO 10993-10). Extracts made from the HSR-modified electrodes were created using either saline or inert oil to examine

© 2024 Pulse Technologies Inc. Advanced Materials Interfaces published by Wiley-VCH GmbH

21967350, 0, Downloaded from https://onlinelibrary.wiley.com/doi/10.1002/admi.202400017, Wiley Online Library on [19/07/2024]. See the Terms and Conditions (https://onlinelibrary.wiley.com/terms-and-conditions) on Wiley Online Library for rules of use; OA articles are governed by the applicable Creative Commons License

both hydrophilic and hydrophobic content release. The results of the cell culture cytotoxicity test system are deemed suitable if the observed responses to the negative control yield grade 0 (no reactivity) and to the positive control at least grade 3 (moderate reactivity). The test article complies with the test requirements if the response to the test article does not exceed grade 2 (mildly reactive). A grade greater than 2 is considered indicative of cytotoxic effects. **Figure 13** presents the results of the cytotoxicity measurements for the restructured Pt10Ir electrodes exposed to fibroblast cells. The negative control demonstrated no response (grade 0), and the positive control triggered severe reactivity (grade 4), confirming the suitability of the test system. The HSR-Pt10Ir electrode test article displayed "slight" cytotoxicity (grade 1), indicated by >20% of rounded cells, loosely attached cells, and cells lacking intracytoplasmic granules, occasional lysed cells, and limited to no growth inhibition. These results were observed across all replicates.

The intracutaneous reactivity test compares levels of erythema and edema at the site of injection of the extracts. The test requirements are deemed satisfactory when the final score is 1.0 or lower. The restructured Pt10Ir electrodes successfully met these requirements, with rabbits treated with the test article extracts having shown no evidence of edema in the injection sites and only minor levels of erythema compared to controls (**Figure 14**). Interestingly, the minor reactions were only observed in neutral-oil extracts, indicating any irritant is likely to be non-polar in nature. Skin sensitization studies were also performed with no evidence of sensitization observed in the guinea pigs treated with the test article, according to the protocols and scoring metrics of the Magnusson & Kligman scale.[132,133] Therefore, we conclude overall that restructured Pt10Ir electrodes are not considered to induce contact dermal allergenicity, or any other significant adverse reaction from these tests.

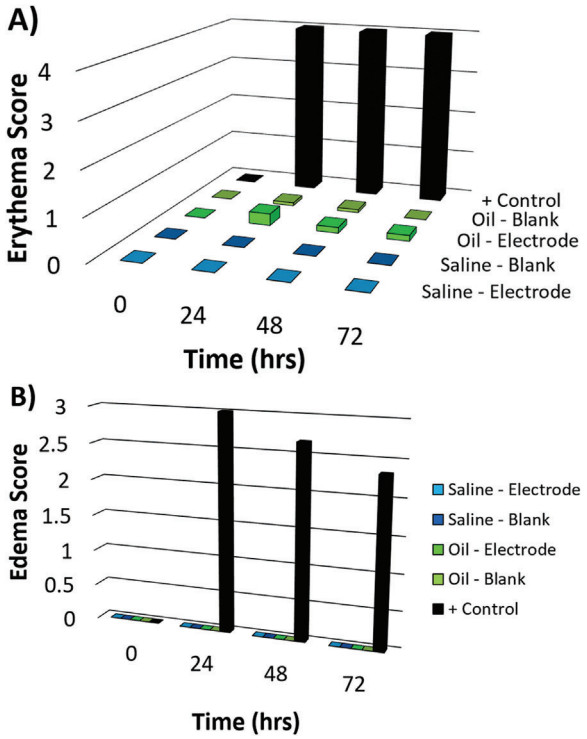

Figure 14. In vivo skin irritation assays. Intradermal irritation in a rabbit model system was evaluated for aqueous and oil-based extracts from restructured Pt10Ir electrodes according to ISO 10993-10(2010). Irritation was determined by evaluating, A) erythema (redness, top panel), and, B) edema (swelling, bottom panel) at the site of injection. Negative controls were vehicle only, while positive controls consisted of 0.1% sodium dodecyl sulfate injections. Data are an average of three injections of each experimental condition per animal across 6 total animals. A version of this figure with error bars has been included in Figure S3 (Supporting Information).

3.5. Concluding Remarks

This report demonstrates for the first time the use of novel femtosecond laser hierarchical surface restructuring (HSR) technology to significantly enhance the electrochemical performance of ultra-thin (<25 µm) Pt10Ir alloy electrodes. By tuning the laser fluence, charge storage capacity and specific capacitance were improved up to 85-fold and 1400-fold, respectively. The HSR process was optimized to maintain a restructuring depth that was significantly less than 20 µm, verified through cross-sectional measurements. The depth of restructuring correlated with improved electrochemical performance, indicating electrode thickness as a constraint to maximum electrochemical performance. We thoroughly characterized and evaluated the surface, sub-surface, morphological, microstructural, and electrochemical properties of the electrodes. EBSD analysis revealed that the restructured ultra-thin Pt10Ir electrodes exhibit fine crystallographic layers parallel to the original surface structure with predominantly <001> and <112> orientations, with small, crystallographic misorientations between layers favoring efficient electron transport. Biocompatibility studies showed no cytotoxicity, sensitization, or irritation in both in vitro and in vivo models. The practicality of the HSR technique was successfully tested on a commercially available cortical microelectrode array with ultra-thin Pt10Ir electrodes. This demonstrated the technique's adaptability to the geometric and material constraints of existing microelectrode arrays without requiring manufacturing process adjustments. The technology developed in this report has the potential to advance the miniaturization and functionality of neural interfacing electrodes and microelectrode arrays with ultra-thin electrode contacts by enhancing their performance, specificity, and selectivity. We acknowledge the need for further long-term studies to characterize electrodes' stability in terms of electrochemical performance and morphology to demonstrate the effectiveness and biocompatibility of ultra-thin HSR electrodes in vivo.

Supporting Information

Supporting Information is available from the Wiley Online Library or from the author.

Conflict of Interest

The authors declare no conflict of interest.

© 2024 Pulse Technologies Inc. Advanced Materials Interfaces published by Wiley-VCH GmbH

21967350, 0, Downloaded from https://onlinelibrary.wiley.com/doi/10.1002/admi.202400017, Wiley Online Library on [19/07/2024]. See the Terms and Conditions (https://onlinelibrary.wiley.com/terms-and-conditions) on Wiley Online Library for rules of use; OA articles are governed by the applicable Creative Commons License

Data Availability Statement

The data that support the findings of this study are available from the corresponding author upon reasonable request.

Keywords

electrodes and microelectrode arrays, femtosecond laser, hierarchical surface restructuring, hierarchical surfaces, neural interfacing, neurostimulation

Received: January 7, 2024
Revised: June 13, 2024
Published online:

[1] D. T. M. Chan, X. L. Zhu, J. H. M. Yeung, V. C. T. Mok, E. Wong, C. Lau, R. Wong, C. Lau, W. S. Poon, *Asian J Surg* **2009**, *32*, 258.
[2] X. Navarro, T. B. Krueger, N. Lago, S. Micera, T. Stieglitz, P. Dario, *J. Peripher. Nerv. Syst.* **2005**, *10*, 229.
[3] J. A. O. Obeso, W. C. Olanow, M. C. Rodriguez-Oroz, P. Krack, R. Kumar, A. E. Lang, *N. Engl. J. Med.* **2001**, *345*, 956.
[4] K. Bazaka, M. Jacob, *Electronics* **2012**, *2*, 1.
[5] N. P. Aryan, M. I. H. B. Asad, C. Brendler, S. Kibbel, G. Heusel, A. Rothermel, in *2011 Annual International Conference of the IEEE Engineering in Medicine and Biology Society*, IEEE, Boston, MA, USA **2011**.
[6] N. Ullah, S. Omanovic, *Mater. Chem. Phys.* **2015**, *159*, 119.
[7] S. F. Cogan, in *Proceedings of the 25th Annual International Conference of the IEEE Engineering in Medicine and Biology Society*, IEEE, Cancun, Mexico **2003**.
[8] A. Prochazka, V. K. Mushahwar, D. B. McCreery, *J Physiol* **2001**, *533*, 99.
[9] S. F. Cogan, *Annu. Rev. Biomed. Eng.* **2008**, *10*, 275.
[10] D. R. Merrill, *Dev Med Child Neurol* **2009**, *51*, 154.
[11] B. Wessling, W. Mokwa, U. Schnakenberg, *J. Micromech. Microeng.* **2006**, *16*, S142.
[12] L. S. Robblee, J. McHardy, J. M. Marston, S. B. Brummer, *Biomaterials* **1980**, *1*, 135.
[13] A. K. Compton, B. Shah, S. M. Hayek, *Curr Pain Headache Rep* **2012**, *16*, 35.
[14] R. S. Taylor, R. J. Taylor, J. P. Van Buyten, E. Buchser, R. North, S. Bayliss, *J Pain Symptom Manage* **2004**, *27*, 370.
[15] J. Grider, *Pain Physician* **2016**, *19*, E33.
[16] B. Linderoth, R. D. Foreman, *Physiology of Spinal Cord Stimulation: Review and Update* **1999**, *2*, 150.
[17] T. Wolter, *J Pain Res* **2014**, *7*, 651.
[18] M. E. Frey, L. Manchikanti, R. M. Benyamin, D. M. Schultz, H. S. Smith, S. P. Cohen, *Pain Physician* **2009**, *12*, 379.
[19] L. J. Epstein, M. Palmieri, *Mt Sinai J Med* **2012**, *79*, 123.
[20] N. Y. Siddiqui, J. M. Wu, C. L. Amundsen, *Neurourol Urodyn* **2010**, *29*, S18.
[21] W. W. Leng, M. B. Chancellor, *Urologic Clinics of North America* **2005**, *32*, 11.
[22] A. J. Malouf, C. J. Vaizey, R. J. Nicholls, M. A. Kamm, *Ann. Surg.* **2000**, *232*, 143.
[23] M. A. Kamm, T. C. Dudding, J. Melenhorst, M. Jarrett, Z. Wang, S. Buntzen, C. Johansson, S. Laurberg, H. Rosen, C. J. Vaizey, K. Matzel, C. Baeten, *Gut* **2010**, *59*, 333.
[24] A. Schmidt Richard, U. Jonas, K. A. Oleson, R. A. Janknegt, M. M. Hassouna, S. W. Siegel, P. E. V. van Kerrebroeck, *J Urol* **1999**, *162*, 352.
[25] M. E. D. Jarrett, G. Mowatt, C M A. Glazener, C. Fraser, R. J. Nicholls, A. M. Grant, M. A. Kamm, *Br J Surg* **2004**, *91*, 1559.
[26] A. Handforth, C. M. DeGiorgio, S. C. Schachter, B. M. Uthman, D. K. Naritoku, E. S. Tecoma, T. R. Henry, S. D. Collins, B. V. Vaughn, R. C. Gilmartin, D. R. Labar, G. L. Morris III, M. C. Salinsky, I. Osorio, R. K. Ristanovic, D. M. Labiner, J. C. Jones, J. V. Murphy, G. C. Ney, J. W. Wheless, *Neurology* **1998**, *51*, 48.
[27] S. C. Schachter, C. B. Saper, *Epilepsia* **1998**, *39*, 677.
[28] R. H. Howland, *Curr Behav Neurosci Rep* **2014**, *1*, 64.
[29] D. T. Plachta, M. Gierthmuehlen, O. Cota, N. Espinosa, F. Boeser, T. C. Herrera, T. Stieglitz, J. Zentner, *J. Neural Eng.* **2014**, *11*, 036011.
[30] G. C. Albert, C. M. Cook, F. S. Prato, A. W. Thomas, *Neurosci Biobehav Rev* **2009**, *33*, 1042.
[31] A. P. Amar, *Expert Rev. Neurother.* **2007**, *7*, 1763.
[32] H. Cagnan, T. Denison, C. McIntyre, P. Brown, *Nat. Biotechnol.* **2019**, *37*, 1024.
[33] G. K. Bergey, *Exp Neurol* **2013**, *244*, 87.
[34] M. Madhavan, S. K. Mulpuru, C. J. McLeod, Y. M. Cha, P. A. Friedman, *J Am Coll Cardiol* **2017**, *69*, 211.
[35] S. K. Mulpuru, M. Madhavan, C. J. McLeod, Y. M. Cha, P. A. Friedman, *J Am Coll Cardiol* **2017**, *69*, 189.
[36] C. L. Witherell, *Critical Care Nursing Clinics of North America* **1994**, *6*, 85.
[37] I. Stevenson, A. Voskoboinik, *Aust J Gen Pract* **2018**, *47*, 264.
[38] P. Halbfass, K. Sonne, K. Nentwich, E. Ene, T. Deneke, *Clin. Res. Cardiol.* **2018**, *107*, 100.
[39] C. P. Lau, C. W. Siu, H. F. Tse, *Circulation* **2014**, *129*, 811.
[40] S. H. Kirwin, *Cochlear Implants : Technological Advances, Psychological/social Impacts and Long-term Effectiveness*, Nova Science Publishers, Inc, Hauppauge, New York **2014**.
[41] D. Fitzpatrick, *Implantable electronic medical devices*, Elsevier, Amsterdam, Netherlands **2014**.
[42] L. Sennaroglu, *Cochlear Implants Int* **2010**, *11*, 4.
[43] M. L. Carlson, C. L. Driscoll, R. H. Gifford, S. O. McMenomey, *Otolaryngol Clin North Am* **2012**, *45*, 221.
[44] C. W. D. Dodds, Y. T. Wong, P. J. Byrnes-Preston, M. Rendl, N. H. Lovell, G. J. Suaning, in *Proceedings of the 4th International IEEE EMBS Conference on Neural Engineering*, IEEE, Antalya, Turkey **2009**.
[45] J. Dowling, *Eye* **2009**, *23*, 1999.
[46] G. J. Suaning, N. H. Lovell, K. Schindhelm, M. T. Coroneo, *Australian and New Zealand Journal of Ophthalmology* **1998**, *26*, 195.
[47] R. K. Shepherd, M. N. Shivdasani, D. A. Nayagam, C. E. Williams, P. J. Blamey, *Trends Biotechnol.* **2013**, *31*, 562.
[48] T. Guenther, N. H. Lovell, G. J. Suaning, *Expert Rev. Med. Devices* **2012**, *9*, 33.
[49] E. M. Maynard, *Annu. Rev. Biomed. Eng.* **2001**, *3*, 145.
[50] J. D. Weiland, M. S. Humayun, *IEEE Eng Med Biol Mag* **2006**, *25*, 60.
[51] E. Krames, P. H. Peckham, A. R. Rezai, *Neuromodulation : comprehensive textbook of principles, technologies, and therapies*, (Eds.:E. Krames, P. H. Peckham, A. R. Rezai), Academic Press, Cambridge, Massachusetts **2018**.
[52] S. Eljamel, K. Slavin, *Neurostimulation : Principles and Practice*, John Wiley & Sons, Hoboken, New Jersey **2013**.
[53] B. Dibner, in *Encyclopedia Britannica* (2023 November 15).
[54] L. Galvani, D. H. D. Roller, *Am. J. Phys.* **1954**, *22*, 40.
[55] J. Ordonez, M. Schuettler, C. Boehler, T. Boretius, T. Stieglitz, *MRS Bull.* **2012**, *37*, 590.
[56] S. Amini, W. Seche, N. May, H. Choi, P. Tavousi, S. Shahbazmohamadi, *Sci. Rep.* **2022**, *12*, 13966.
[57] J. X. J. Zhang, K. Hoshino, *Molecular Sensors and Nanodevices*, Academic Press, Cambridge, Massachusetts **2019**, pp. 489–545.
[58] J. Kilby, K. Prasad, G. Mawston, *IEEE Sens. J.* **2016**, *16*, 5510.
[59] P. A. Grandjean, J. T. Mortimer, *Ann. Biomed. Eng.* **1986**, *14*, 53.
[60] W. D. Memberg, P. H. Peckham, M. W. Keith, *IEEE Transactions on Rehabilitation Engineering* **1994**, *2*, 80.

© 2024 Pulse Technologies Inc. Advanced Materials Interfaces published by Wiley-VCH GmbH

21967350, 0, Downloaded from https://onlinelibrary.wiley.com/doi/10.1002/admi.202400017, Wiley Online Library on [19/07/2024]. See the Terms and Conditions (https://onlinelibrary.wiley.com/terms-and-conditions) on Wiley Online Library for rules of use; OA articles are governed by the applicable Creative Commons License

[61] J. M. Akers, P. H. Peckham, M. W. Keith, K. Merritt, *IEEE Transactions on Rehabilitation Engineering* **1997**, *5*, 207.
[62] NIH, "Cochlear Implants", The National Institute on Deafness and Other Communication Disorders (NIDCD), NIH Publication No. 00-4798, 2016.
[63] S. K. Kelly, D. B. Shire, J. Chen, P. Doyle, M. D. Gingerich, S. F. Cogan, W. A. Drohan, S. Behan, L. Theogarajan, J. L. Wyatt, J. F. Rizzo III, *IEEE Trans. Biomed. Eng.* **2011**, *58*, 3197.
[64] Y. Cho, J. Park, C. Lee, S. Lee, *Bioelectron Med* **2020**, *6*, 23.
[65] E. H. Rijnbeek, N. Eleveld, W. Olthuis, *Front Neurosci* **2018**, *12*, 350.
[66] C. Russell, A. D. Roche, S. Chakrabarty, *Int J Intell Robot Appl* **2019**, *3*, 11.
[67] M. O. Adedoyin, P. T. Ohara, L. Jasmin, *Encyclopedia of Pain*, Springer, Berlin Heidelberg **2013**, pp. 509–515.
[68] D. Bansal, R. Mahajan, *EEG-Based Brain-Computer Interfaces* (Eds.: D. Bansal, R. Mahajan), Academic Press, Cambridge, Massachusetts **2019**, pp. 21–71.
[69] P. Leleux, C. Johnson, X. Strakosas, J. Rivnay, T. Hervé, R. M. Owens, G. G. Malliaras, *Adv. Healthcare Mater.* **2014**, *3*, 1377.
[70] I. Jones, M. I. Johnson, *Continuing Education in Anaesthesia Critical Care & Pain* **2009**, *9*, 130.
[71] T. Keller, A. Kuhn, *Journal of Automatic Control* **2008**, *18*, 35.
[72] P. E. Barkhaus, S. D. Nandedkar, *Muscle Nerve* **1994**, *17*, 1317.
[73] G. E. Loeb, R. A. Peck, *J Neurosci Methods* **1996**, *64*, 95.
[74] R. A. Normann, E. Fernandez, *J. Neural Eng.* **2016**, *13*, 061003.
[75] R. Sahyouni, A. Mahmoodi, J. W. Chen, D. T. Chang, O. Moshtaghi, H. R. Djalilian, H. W. Lin, *Neurosurg Rev* **2019**, *42*, 227.
[76] S. Uematsu, R. Lesser, R. Fisher, G. Krauss, J. Hart, E. P. Vining, J. Freeman, B. Gordon, *Stereotact Funct Neurosurg* **1990**, *54*, 34.
[77] G. Schalk, E. C. Leuthardt, *IEEE Rev Biomed Eng* **2011**, *4*, 140.
[78] T. Stieglitz, E. M. Hol, I. Huitinga, J. Wijnholds, A. B. Bergen, G. J. Boer, D. F. Swaab, in *Neurotherapy: Progress in Restorative Neuroscience and Neurology Progress in Brain Research*, Elsevier, Amsterdam, Netherlands **2009**.
[79] M. L. Homer, A. V. Nurmikko, J. P. Donoghue, L. R. Hochberg, *Annu. Rev. Biomed. Eng.* **2013**, *15*, 383.
[80] G. S. Brindley, *J Physiol* **1972**, *222*, 135.
[81] G. S. Brindley, C. E. Polkey, D. N. Rushton, *J. Spinal Cord Med.* **1982**, *20*, 365.
[82] G. S. Brindley, C. E. Polkey, D. N. Rushton, L. Cardozo, *J Neurol Neurosurg Psychiatry* **1986**, *49*, 1104.
[83] G. He, X. Dong, M. Qi, *Mater. Res. Express* **2020**, *7*, 102001.
[84] R. Saigal, C. Renzi, V. K. Mushahwar, *IEEE Trans. Neural Syst. Rehabil. Eng.* **2004**, *12*, 430.
[85] V. K. Mushahwar, D. F. Collins, A. Prochazka, *Exp Neurol* **2000**, *163*, 422.
[86] P. R. Kennedy, *J Neurosci Methods* **1989**, *29*, 181.
[87] J. C. Williams, R. L. Rennaker, D. R. Kipke, *Brain Res Brain Res Protoc* **1999**, *4*, 303.
[88] S. N. Flesher, J. L. Collinger, S. T. Foldes, J. M. Weiss, J. E. Downey, E. C. Tyler-Kabara, S. J. Bensmaia, A. B. Schwartz, M. L. Boninger, R. A. Gaunt, *Sci. Transl. Med.* **2016**, *8*, 361ra141.
[89] P. K. Campbell, K. E. Jones, R. J. Huber, K. W. Horch, R. A. Normann, *IEEE Trans. Biomed. Eng.* **1991**, *38*, 758.
[90] D. R. Kipke, R. J. Vetter, J. C. Williams, J. F. Hetke, *IEEE Trans. Neural Syst. Rehabil. Eng.* **2003**, *11*, 151.
[91] J. D. Simeral, S. P. Kim, M. J. Black, J. P. Donoghue, L. R. Hochberg, *J. Neural Eng.* **2011**, *8*, 025027.
[92] N. Maling, S. F. Lempka, Z. Blumenfeld, H. Bronte-Stewart, C. C. McIntyre, *J Neurophysiol* **2018**, *120*, 1932.
[93] C. R. Butson, C. C. McIntyre, *Brain Stimul.* **2008**, *1*, 7.
[94] G. Kunkel, J. R. Leger, *IEEE J. Quantum Electron.* **2019**, *55*, 1600108.
[95] K.-H. Ok, J. Kim, S.-R. Park, Y. Kim, C.-J. Lee, S.-J. Hong, M.-G. Kwak, N. Kim, C. J. Han, J.-W. Kim, *Sci. Rep.* **2015**, *5*, 9464.
[96] C. M. Elder, T. Hashimoto, J. Zhang, J. L. Vitek, *J Neurosci Methods* **2005**, *142*, 11.
[97] D. McCreery, A. Lossinsky, V. Pikov, X. Liu, *IEEE Trans. Biomed. Eng.* **2006**, *53*, 726.
[98] H. S. Sohal, G. J. Clowry, A. Jackson, A. O'Neill, S. N. Baker, *PLoS One* **2016**, *11*, 0165606.
[99] M. Shokoueinejad, D.-W. Park, Y. H. Jung, S. K. Brodnick, J. Novello, A. Dingle, K. I. Swanson, D.-H. Baek, A. J. Suminski, W. B. Lake, Z. Ma, J. Williams, *Micromachines* **2019**, *10*, 62.
[100] M. Jorfi, J. L. Skousen, C. Weder, J. R. Capadona, *J. Neural Eng.* **2015**, *12*, 011001.
[101] A. F. Renz, J. Lee, K. Tybrandt, M. Brzezinski, D. A. Lorenzo, M. C. Cheraka, J. Lee, F. Helmchen, J. Vörös, C. M. Lewis, *Adv. Healthcare Mater.* **2020**, *9*, 2000814.
[102] R. A. Green, P. B. Matteucci, C. W. D. Dodds, J. Palmer, W. F. Dueck, R. T. Hassarati, P. J. Byrnes-Preston, N. H. Lovell, G. J. Suaning, *J. Neural Eng.* **2014**, *11*, 056017.
[103] R. A. Green, N. H. Lovell, G. G. Wallace, L. A. Poole-Warren, *Biomaterials* **2008**, *29*, 3393.
[104] G. Taylor, J. Shallenberger, S. Tint, A. Fones, H. Hamilton, L. Yu, S. Amini, J. Hettinger, *Surf. Coat. Technol.* **2021**, *426*, 127803.
[105] G. Taylor, R. Paladines, A. Marti, D. Jacobs, S. Tint, A. Fones, H. Hamilton, L. Yu, S. Amini, J. Hettinger, *Electrochim. Acta* **2021**, *394*, 139118.
[106] N. Page, J. Lucchi, J. Buchan, A. Fones, H. Hamilton, T. Scabarozi, L. Yu, S. Amini, J. Hettinger, *Mater. Today Commun.* **2021**, *29*, 102967.
[107] H. Khosla, W. Seche, D. Ammerman, S. Elyahoodayan, G. A. Caputo, J. Hettinger, S. Amini, G. Feng, *Sci. Rep.* **2023**, *13*, 19778.
[108] I. Gablech, E. D. Głowacki, *Adv. Electron. Mater.* **2023**, *9*, 2300258.
[109] S. Meijs, M. Fjorback, C. Jensen, S. Sorensen, K. Rechendorff, N. J. Rijkhoff, *Front Neurosci* **2015**, *9*, 268.
[110] S. J. Wilks, S. M. Richardson-Burns, J. L. Hendricks, D. C. Martin, K. J. Otto, *Front. Neuroeng.* **2009**, *2*, 591.
[111] H. Park, P. Takmakov, H. Lee, *Sci Rep* **2018**, *8*, 4375.
[112] S. F. Cogan, J. Ehrlich, T. D. Plante, A. Smirnov, D. B. Shire, M. Gingerich, J. F. Rizzo, *J Biomed Mater Res B Appl Biomater* **2009**, *89*, 353.
[113] K. Bazaka, M. V. Jacob, *Electronics* **2013**, *2*, 1.
[114] M. Mohammed, N. Ivica, H. Bjartmarz, P. T. Thorbergsson, L. M. E. Pettersson, J. Thelin, J. Schouenborg, *J Neurosci Methods* **2022**, *365*, 109399.
[115] H. A. C. Wark, K. S. Mathews, R. A. Normann, E. Fernandez, *J. Neural Eng.* **2014**, *11*, 046027.
[116] A. T. Connolly, R. J. Vetter, J. F. Hetke, B. A. Teplitzky, D. R. Kipke, D. S. Pellinen, D. J. Anderson, K. B. Baker, J. L. Vitek, M. D. Johnson, *IEEE Trans. Biomed. Eng.* **2016**, *63*, 148.
[117] F. Steigerwald, C. Matthies, J. Volkmann, *Neurotherapeutics* **2019**, *16*, 100.
[118] M. F. Contarino, L. J. Bour, R. Verhagen, M. A. J. Lourens, R. M. A. de Bie, P. van den Munckhof, P. R. Schuurman, *Neurology* **2014**, *83*, 1163.
[119] L. Li, C. Jiang, W. Duan, Z. Wang, F. Zhang, C. He, T. Long, L. Li, *Microsyst. Nanoeng.* **2022**, *8*, 96.
[120] MHLW (Ministry of Health, Labour and Welfare,) MHLW (Ministry of Health, Labour and Welfare, Japan), "Guidelines for preclinical biological evaluation of medical materials and devices", JIMUREN-RAKU Iryokiki-Shinsa, vol. *36*, **2003**.
[121] R. Phillip, M. Zahid, L. Shang, **2016**.
[122] E. Lourenço, J. A. Cortês, J. Costa, A. B. R. Linhares, G. Alves, *Key Engineering Materials* **2014**, *631*, 357.

© 2024 Pulse Technologies Inc. Advanced Materials Interfaces published by Wiley-VCH GmbH

21967350, 0, Downloaded from https://onlinelibrary.wiley.com/doi/10.1002/admi.202400017, Wiley Online Library on [19/07/2024]. See the Terms and Conditions (https://onlinelibrary.wiley.com/terms-and-conditions) on Wiley Online Library for rules of use; OA articles are governed by the applicable Creative Commons License

[123] B. L'Azou, J. Jorly, D. On, E. Sellier, F. Moisan, J. Fleury-Feith, J. Cambar, P. Brochard, C. Ohayon-Courtès, *Part. Fibre Toxicol.* **2008**, *5*, 22.
[124] J. D. Weiland, D. J. Anderson, M. S. Humayun, *IEEE Trans. Biomed. Eng.* **2002**, *49*, 1574.
[125] X. T. Cui, D. D. Zhou, *IEEE Trans. Neural Syst. Rehabil. Eng.* **2007**, *15*, 502.
[126] Z. J. Du, X. Luo, C. Weaver, X. T. Cui, *J Mater Chem C Mater* **2015**, *3*, 6515.
[127] S. Negi, R. Bhandari, L. Rieth, F. Solzbacher, *Biomed. Mater.* **2010**, *5*, 015007.
[128] S. F. Cogan, P. R. Troyk, J. Ehrlich, T. D. Plante, *IEEE Trans. Biomed. Eng.* **2005**, *52*, 1612.
[129] Q. Zeng, K. Xia, B. Sun, Y. Yin, T. Wu, M. S. Humayun, *Electrochim. Acta* **2017**, *237*, 152.
[130] E. Slavcheva, R. Vitushinsky, W. Mokwa, U. Schnakenberg, *J. Electrochem. Soc.* **2004**, *151*, E226.
[131] H. Jang, J. Lee, *J Energy Chem* **2020**, *46*, 152.
[132] E. Schlede, R. Eppler, *Contact Dermatitis* **1995**, *32*, 1.
[133] B. Magnusson, A. M. Kligman, *J. Invest. Dermatol.* **1969**, *52*, 268.

© 2024 Pulse Technologies Inc. Advanced Materials Interfaces published by Wiley-VCH GmbH

21967350, 0, Downloaded from https://onlinelibrary.wiley.com/doi/10.1002/admi.202400017, Wiley Online Library on [19/07/2024]. See the Terms and Conditions (https://onlinelibrary.wiley.com/terms-and-conditions) on Wiley Online Library for rules of use; OA articles are governed by the applicable Creative Commons License